Engineering Structures 248 (2021) 113063

Contents lists available at ScienceDirect

Engineering Structures

journal homepage: www.elsevier.com/locate/engstruct

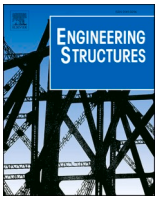

Experimental study of sliding friction damper with composite materials for earthquake resistant structures

Martina Paronesso, Dimitrios G. Lignos *

École Polytechnique Fédérale de Lausanne, EPFL, Resilient Steel Structures Laboratory, RESSLab, Station 18, CH 1015 Lausanne, Switzerland

ARTICLE INFO

Keywords:
Friction damper
Friction coefficient
Supplemental damping
Composite materials
Wear
Earthquake engineering

ABSTRACT

This paper presents the experimental results from 62 tests on five non-metallic friction pads that could be potentially used in friction dampers for minimizing earthquake-induced damage in buildings. The friction pads are composed of fibres and organic and inorganic fillers bounded together by phenolic resins and have never been explored for potential use in supplemental damping devices. A full-scale sliding friction damper prototype was developed for this purpose. Parameters examined as part of the experimental program include the applied pressure level to control the sliding force, the imposed loading protocol and the associated loading rate. The experimental results reveal that two of the explored friction pads exhibit similar static and dynamic friction coefficients, which are on the order of 0.2 and 0.3 regardless of the examined pressure level and loading protocol. These values are fairly invariant with respect to temperature and to sliding velocity as long as it is larger than 10 mm/s. While surface wear is the primary damage mechanism of the two most prominent friction pads, their immediate replacement is not imperative in typical earthquake mainshock-aftershock sequences. Moreover, loss of bolt pretension in the friction damper was practically negligible during the same loading sequences.

1. Introduction

During the past four decades, several passive control devices have been developed to enhance the seismic performance of buildings by providing supplemental damping [1,2]. Commonly used devices include yield, viscous and friction dampers. Yield dampers, such as buckling-restrained braces, deliver an appreciable energy dissipation capacity [3–5]. However, the steel core of buckling-restrained braces exhibits cyclic hardening. Therefore, the use of overstrength factors to design the non-dissipative structural elements of a building is imperative. Concerns regarding potential residual deformations and soft-storey mechanisms in the aftermath of earthquakes have also been raised [6,7]. Viscous dampers are sensitive to temperature and imposed velocity [8–10]. Therefore, they may exert forces that are influenced by the dynamic load imposed on a building.

Friction dampers, if engineered properly, they are not prone to the aforementioned issues [11,12]. Over the years, numerous types of friction dampers have been developed to enhance the seismic performance of buildings. Pall [13] developed limited slip bolted joints to control the seismic response of structures. Subsequent studies have investigated the use of friction spring dampers [14] and sliding friction dampers in steel frames with X-bracing [15–17] as well as chevron bracing [18] configurations. In [19], seven different passive energy dissipation systems were tested on a large-scale 9-storey steel frame. Among the tested devices, Sumitomo friction dampers were effective in providing a stable force–displacement hysteretic response under earthquake shaking. Slotted bolted connections [20–24] and rotational bolted links [25–27] have also been used in steel concentrically braced frames and eccentrically braced frames, respectively. Prior work has also been conducted on the use of friction pads in beam-to-column friction joints of steel moment resisting frames [23,28–30] as well as reinforced concrete structures [31]. Similarly, friction devices have been employed in self-centering beam-to-column joints [32,33] and steel column bases [34,35].

The energy dissipation capacity of a friction damper relies on the friction properties of the materials utilized as pads. In this regard, several experimental investigations have been conducted on different friction pad types. Particularly, prior work has focused on mild-steel pads [13,21,36–38]. Due to surface wear, these may exhibit an unstable force–displacement hysteretic response under cyclic loading. Others have explored the potential use of brass pads [21,36,38–40]. Their hysteretic response is found to be more stable compared to their mild-

* Corresponding author.
E-mail addresses: martina.paronesso@epfl.ch (M. Paronesso), dimitrios.lignos@epfl.ch (D.G. Lignos).

https://doi.org/10.1016/j.engstruct.2021.113063
Received 18 April 2021; Received in revised form 7 July 2021; Accepted 18 August 2021

steel counterparts. However, galvanic corrosion may be a challenge to overcome. Further investigations have been conducted on steel plates coated with sprayed aluminium [38,41,42]. This solution could provide a fairly stable force–displacement hysteretic response of the friction device. However, the obtained friction coefficients are somewhat pressure-dependent. Moreover, the application process of the coating is non-trivial. Indeed, it usually requires specialized equipment to ensure a high-quality control and performance of the coated steel plates and associated sliding interfaces. As such, the overall cost of the friction pad may be improper. Wolff [43] investigated the use of stainless steel plates coated with non-asbestos organic (NAO) materials in base isolation systems. The NAO materials, which exhibit a stable force–displacement hysteretic response, provide friction coefficients lower than 0.2. Similar findings hold true for NAO pads when tested with mild and stainless steel interfaces [44,32].

In more recent work, the use of Bissaloy steel pads has been explored [36,37,45]. Their hysteretic response is fairly stable and repeatable. Surface wear, in this case, is fairly minimal. However, Golondrino et al. [45] found that these materials may provide friction coefficients lower than 0.2 for tightening torques ranging between 350 N.m and 500 N.m. In more recent works [38,46], the use of non-metallic materials has been explored. These studies suggest that a handful of these materials could exhibit a stable hysteretic response under uniaxial cyclic displacement histories. The friction coefficient of these materials, which is both pressure- and velocity-independent, assumes values close to 0.2 [38]. A potential benefit of non-metallic friction pads is that they are not susceptible to galvanic corrosion. Although promising, only a few experimental studies have explored the use of these pad types in sliding friction dampers.

This paper characterizes the behaviour of a broad range of non-metallic composite materials. The selected materials are readily available on the market at a fairly minimal cost. Their performance is investigated through a sliding friction damper prototype, which was designed and developed by the authors. The experimental program is conducted under two pressure levels. Monotonic and cyclic tests are conducted at different loading rates aiming to investigate their effect on the force–displacement response of the sliding friction damper. Furthermore, pulse-like and mainshock-aftershock loading protocols are carried out in order to test the sliding friction damper under conditions similar to those occurring during a seismic event. The evolution of the static and dynamic friction coefficients is examined by monitoring both the sliding force and bolt preload. Similarly, temperature variations are tracked close to the sliding interface in order to investigate the effect of the latter on the friction properties of the pads. Limitations as well as suggestions for future work are discussed.

2. Description of the Experimental Campaign

2.1. Sliding Friction Damper Prototype

Fig. 1 illustrates the main components of the sliding friction damper. It consists of four types of metal plates made of S355 J2 steel (nominal yield stress, $f_y = 355$ MPa) and standard manufacturing tolerances. These types include (i) end steel plates ($t = 40$ mm), which are positioned at the damper ends and are equipped with ball joints; (ii) an inner slotted steel plate ($t = 40$ mm); (iii) fixed outer steel plates ($t = 20$ mm), which connect one of the end plates to the inner slotted plate; and (iv) sliding outer plates ($t = 20$ mm). These connect one of the end plates to the slotted holes of the inner plate. Each plate has a width of 220 mm and standard 26 mm diameter holes. The sliding motion occurs between two friction pads and the inner slotted plate. At this location, the clamping force is applied with six preloaded high-strength M24 bolts 10.9 class (nominal ultimate stress, $f_{ub} = 1000$ MPa). Disc spring washers (SCHNORR, $\Phi_i = 25$ mm, $\Phi_e = 56$ mm, $h = 7.75$ mm, $t = 6$ mm) are used to minimize pretension variations during the sliding motion as suggested in [38,46]. A further six preloaded high-strength M24 bolts 10.9 class ($f_{ub} = 1000$ MPa) are utilized to joint the fixed outer plates to the inner slotted plate. A pinned connection is realized at the damper ends through two high-strength steel pins (ETG 100, $f_y \geq 865$ MPa). A ball joint SKF GE 50 ESX-2LS ($\Phi_i = 50$ mm, $\Phi_e = 75$ mm) is placed around each pin in order to accommodate potential relative movements between the latter and the steel plates (see Fig. 1b).

The damper is designed according to [47,48] for a maximum axial force of 450 kN and a maximum axial displacement of ±100 mm. Referring to Fig. 1c, its total length varies from 1500 mm to 1726 mm. The expected slip load is estimated by using Coulomb's law of friction [49]:

$$F_s = n_s \cdot \mu_s \cdot N_{tot} \quad (1)$$

Referring to Fig. 1d, F_s is the slip load (i.e., static friction force), n_s is the number of slip interfaces (i.e., $n_s = 2$), μ_s is the static friction coefficient characterising the friction pad and N_{tot} is the total applied normal force through the preloaded bolts (i.e., $N_{tot} = 6 \cdot N_{bolt}$).

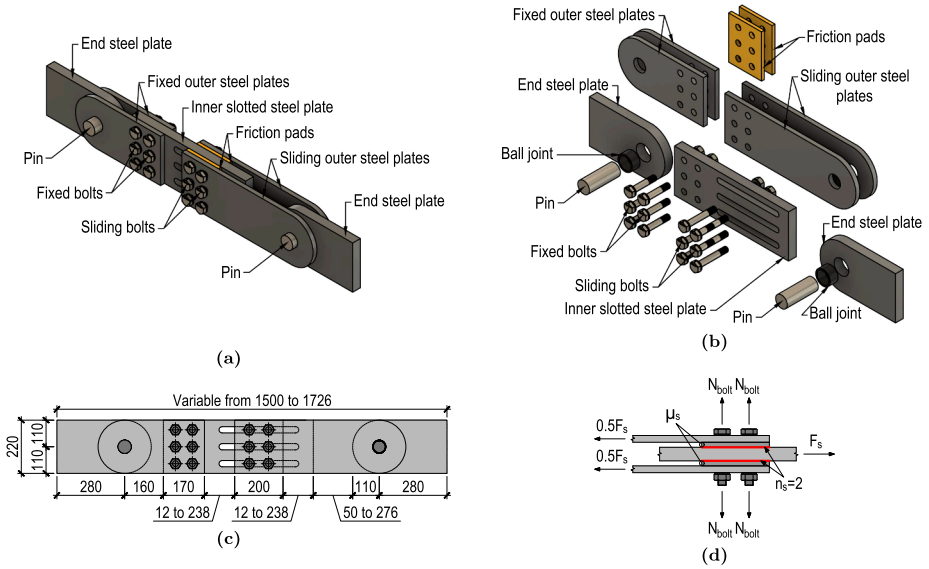

Fig. 1. Sliding friction damper prototype: (a)-(b) basic components, (c) main dimensions in millimetres, (d) parameters used to control the slip load F_s.

2.1.1. Performance Considerations for Selected Friction Pads

The selection of the friction pad materials was based on the following performance criteria, which were established as part of a broader research project with emphasis on the enhanced seismic behaviour of steel braced frame buildings equipped with friction dampers:

- The static friction coefficient μ_s of the pads should ideally be between 0.20 and 0.30 in order to limit the number of preloaded bolts to achieve a desired slip load F_s (see Eq. 1). This, in turn, affects the dimensions of the friction damper.
- During sliding, the steel plates in contact with the friction pads should experience minimal damage due to wear. For this purpose, the hardness of the friction pads shall be lower than the one of the steel plates [50]. This requirement aims at concentrating damage in the replaceable components of the damper in the aftermath of earthquakes.
- Under cyclic loading, the friction damper should exhibit a stable hysteretic response without slip force variations under cyclic loading. For this purpose, the static (μ_s) and dynamic (μ_d) friction coefficients of the pads should be similar [50]. Furthermore, in order to limit surface wear, the hardness of the pads should be lower compared to that of the S355 steel plates [50], which generally ranges between 146 HB and 187 HB.
- Galvanic corrosion at the slip interfaces shall be avoided; therefore, non-metallic composite friction pads are preferable.
- Ideally, the selected friction pads should be readily available on the market and obtainable at minimal costs.

Fig. 2 illustrates the five selected friction pads for the experimental program. According to the manufacturer specifications, they are composed of fibres and organic and inorganic fillers bounded together by phenolic resins. Furthermore, they provide a friction coefficient larger than 0.30 under a maximum operation pressure of 1 MPa. Additional information regarding pertinent material properties is summarized in Table 1. Interestingly, the hardness of M2 and M3 is expressed in the Shore D scale, whereas the Rockwell scale is adopted for the other pads. The Shore hardness method is typically used to measure the hardness of soft materials (e.g. rubbers, elastomers and soft plastics such as polypropylene). On the contrary, the Rockwell hardness method is commonly utilized to determine the hardness of harder plastics such as polycarbonate. This indicates that M2 and M3 are softer materials compared to M1, M4 and M5. Furthermore, the largest values of tensile/flexural strength are observed for the materials M1 and M3.

The recommended operating limits for M4 are 1.7 MPa of pressure and 17.8 m/s of rubber speed, whereas this information was not provided for the rest of the friction pads by the manufacturers. The above limits are only recommended for the intended use and they are far different from those expected in seismic applications (e.g. pressure levels larger than 2.0 MPa). Therefore, an experimental campaign was conducted in order to characterize the behaviour of the selected pads under the operation conditions of interest after coordination with the manufacturers of the pads.

Each pad is 15 mm thick and 200 mm wide. The corresponding heights ranges from 200 mm for M1 and M5 to 220 mm for the rest (see Fig. 2f). For materials M2 and M3, the 26 mm diameter holes were drilled at the EPFL's Structures Laboratory with a water jet cutting machine, whereas the other pads were directly provided with the holes by the manufacturers.

2.2. Laboratory Test Setup and Instrumentation

The experimental program was carried out under displacement control by means of a universal 1 MN servo hydraulic Schenck machine. Its maximum stroke is equal to 250 mm. Referring to Fig. 3a, the friction damper was clamped at both extremities with a maximum pressure of 490 bars. First, the lower half of the damper (i.e., one of the two end plates, the two fixed outer plates and the inner slotted plate) was assembled on a table. Six preloaded M24 bolts 10.9 class were utilized to connect the sliding outer plates to the slotted holes of the inner plate. Finally, the vertical alignment of the damper was verified with the cross-line laser.

Fig. 3b shows the instrumentation of the sliding friction damper. In total, 15 sensors were utilized. The damper's axial force was measured with the load cell of the Schenck machine, whereas the axial displacement was measured with two linear variable differential transformers (LVDTs) located on the fixed and sliding outer steel plates of the damper (LVDTv-W and LVDTv-E). Three additional LVDTs were used to monitor the in-plane and out-of-plane movements of the damper (LVDTh-WE, LVDTh-W-NS, LVDTh-E-NS), whereas two inclinometers (INCs) were utilized to measure the in-plane and out-of-plane rotations (INC-WE, INC-NS) of the damper. Thermocouples (THs) were used to track temperature variations at the surface of the inner slotted plate (THout) as well as close to the sliding interfaces (THbolt). Furthermore, a washer load cell (WLC) was used to verify if pretension variations occur during the sliding motion and to get a sense of the applied bolt preload prior to testing.

2.3. Loading Protocols

The experimental program is described in Table 2. Monotonic (M) and cyclic tests with constant (CA), increasing (IA, IA-H, IA-HH) and decreasing (DA) amplitudes were conducted at different loading rates (i.e., 0.025 Hz, 0.05 Hz and 0.15 Hz) (see Fig. 4a-d). Furthermore, loading protocols idealizing a pulse (PL) and a mainshock-aftershock (MS-AS) series were carried out in order to test the friction damper under conditions similar to those occurring during a seismic event (see Figs. 4e-f). For these tests, the maximum sliding velocity (i.e., 27 mm/s) and the excursion associated to it were constrained by the maximum capacity of the available servo-hydraulic equipment.

In order to examine the response of the friction damper to conditions potentially similar to earthquake loading, of interest are ground motions representing ground shaking in the forward directivity region of a fault rupture. These records are usually characterized by a large high-velocity pulse early on in the ground motion history. Due to limitations of the employed servo-hydraulic equipment and to maximize the input pulse velocity to further evaluate the effects of loading rate on the behaviour of the friction pads, the concept of pulse idealization was employed, which was introduced by [54] to represent near-fault ground motions with reasonable accuracy. The pulse duration herein was tuned to represent the local seismicity characteristics of pulse-like ground motions in Sion (Switzerland). Moreover, other records with similar characteristics were reviewed from historic earthquake data [55].

Referring to Table 2, the loading protocols M, CA, IA, DA and IA-H were run for an expected slip load of 150 kN (i.e., pressure of 5.5 N/mm^2-10 N/mm^2) and 300 kN (i.e., pressure of 7.0 N/mm^2-21 N/mm^2) in order to verify if the friction coefficient μ of the pads is pressure-dependent. The remaining tests (i.e., IA-HH, PL and MS-AS) were performed merely on M1 and M4 for $F_{s,exp} = 300$ kN. The target $F_{s,exp}$ values were achieved by calibrating the bolt preload through a conventional torque wrench.

3. Experimental Results

The experimental results are summarized in three sub-sections. First, the data obtained under the linear loading protocol are reported for $F_{s,exp} = 150$ kN and $F_{s,exp} = 300$ kN. Notably, the performance of the friction damper is evaluated in terms of axial force-axial displacement (F-δ), whereas the bolt prealod N_{bolt} and the friction coefficient μ of the pads are reported as a function of the total cumulative displacement $\sum \delta_i$. The second and third sub-sections include a qualitative and quantitative discussion of the experimental results, respectively.

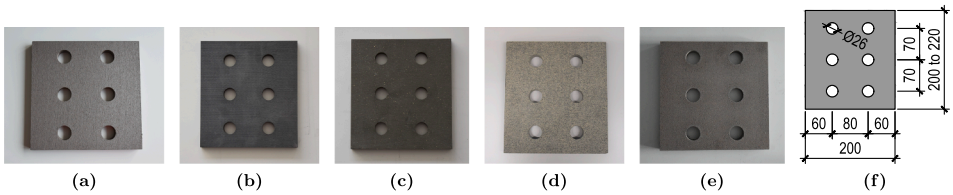

Fig. 2. Friction pads: (a) M1, (b) M2, (c) M3, (d) M4, (e) M5, (f) main dimensions in millimetres.

Table 1
Characteristic properties of the tested friction pad materials.

Material ID	Original application	Friction coefficient[a]					Hardness	Wear rate	Tensile stress[e]	Compressive stress[e]	Normal stress due to flexure[e]
		μ[b]	μ_s	μ_d	P_{ref} [MPa]	T_{ref} [°C]		[10^{-5}mm^3/J]	[MPa]	[MPa]	[MPa]
M1	SID[c]	–	0.36	0.32	1.0	100	73HR	1.0	–	100	67
M2	BA[d]	0.3	–	–	1.0	50	60/70 ShoreD	0.60mm	13.7–17.7	28.4–36.8	–
M3	BA[d]	0.28	–	–	1.0	25	65/75 ShoreD	0.46mm	171.7	–	–
M4	BA[d]	0.59	–	–	1.0	–	104HR	2.3	14.8	73.1	28.3
M5	BA[d]	–	0.67	0.42	1.0	100	97HR	4.5	–	100	52

[a] Friction coefficients obtained under the reference pressure P_{ref} and at the reference temperature T_{ref}
[b] Average friction coefficient
[c] Seismic isolation devices
[d] Braking applications
[e] The tensile stress, compressive stress and normal stress due to flexure of the materials were determined according to [51–53] respectively

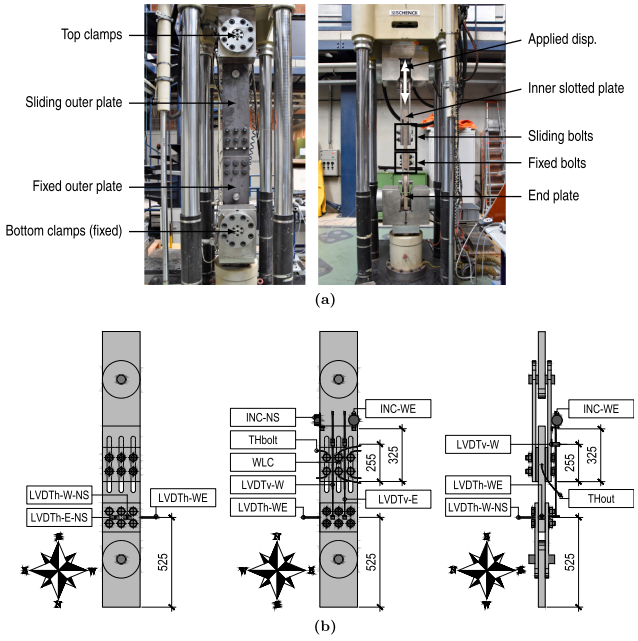

Fig. 3. (a) Sliding friction damper after installation, (b) instrumentation plan.

The friction coefficients reported in the following sections were determined as follows:

$$\mu = \frac{F}{n_s \cdot n_{bolt} \cdot N_{bolt} \cdot (1-\alpha)} \quad (2)$$

Where, n_{bolt} is the number of preloaded bolts (i.e., $n_{bolt} = 6$), N_{bolt} is the bolt preload applied with the wrench torque before each test and α is the loss of pretension measured with the washer load cell. It is noteworthy that μ assumes negative/positive values when the axial force F induces tension/compression on the damper. Furthermore, prior to testing, several calibrations were conducted with the torque wrench in order to ensure that all bolts were equally preloaded. This also included calibration of the washer load cell. Because disc spring washers were employed, variations in bolt pretension were minimized, thus enabling

Table 2
Load protocols used to test the five friction pads.

Loading protocol ID	Disp. amp. [mm]	Frequency f [Hz]	Number of cycles	Sliding velocity v_s [mm/s]
Linear static loading (M)	± 70	0.0025	0.5	0.7
Cyclic loading with constant amplitude (CA)	± 50	0.025	20	5
Cyclic loading with increasing amp. at low rate (IA)	± 5, 10, 15, …, 50	0.025	20	0.5, 1.0, 1.5, …, 5.0
Cyclic loading with decreasing amp. at low rate (DA)	± 50, 45, 40, …, 5	0.025	20	5.0, 4.5, 4.0, …, 0.5
Cyclic loading with increasing amp. at moderate rate (IA-H)	± 5, 10, 15, …, 50	0.05	20	1.0, 2.0, 3.0, …, 10
Cyclic loading with increasing amp. at high rate[a] (IA-HH)	± 5, 10, 15, …, 50	0.15	20	3.0, 6.0, 9.0, …, 30
Pulse-like loading protocol[a] (PL)	50[b]	–	–	50[c]
Mainshock-aftershock protocol[a] (MS-AS):				
- Mainshock (MS)	40[b]	–	–	27[c]
- First aftershock (AS1)	30[a]	–	–	27[c]
- Second aftershock (AS2)	24[b]	–	–	27[c]

[a] Load protocol used to test exclusively the friction pads M1 and M4
[b] Excursion associated to the maximum sliding velocity applied during the load protocol
[c] Maximum sliding velocity applied during the load protocol

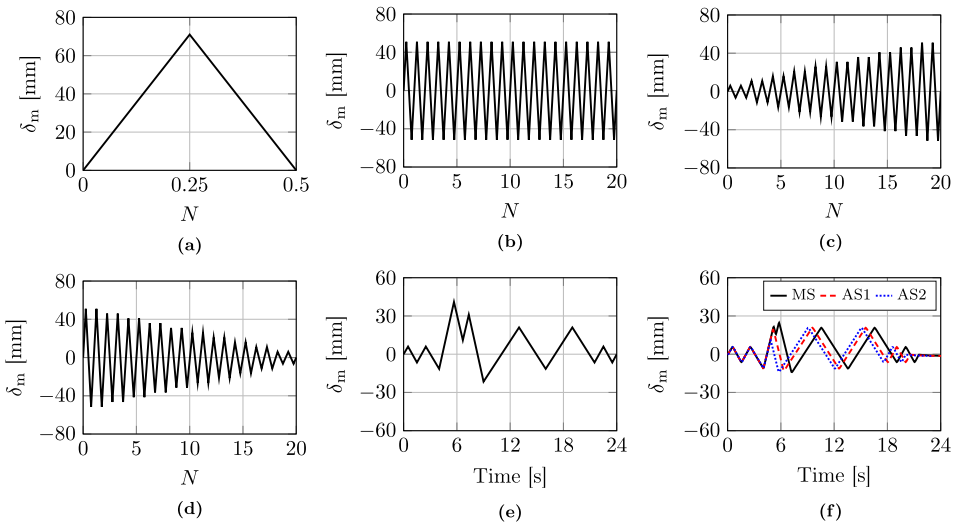

Fig. 4. Employed loading protocols: (a) linear static loading (M), (b) cyclic loading with constant amplitude (CA), (c) cyclic loading with increasing amplitude at low (IA), moderate (IA-H) and high rate (IA-HH), (d) cyclic loading with decreasing amplitude at low rate (DA), (e) pulse-like loading protocol (PL), (f) mainshock-aftershock loading protocol (MS-AS).

the use of only one washer load cell to trace potential bolt relaxations.

3.1. Results obtained under the Linear Static Loading Protocol

The normal pressure levels applied on the friction pads range between 5.5 MPa and 21 MPa. In order to examine the effect of pressure on the friction properties of the pads, a preliminary test was conducted by applying a tightening torque T_{bolt} of 200 Nm/bolt and the loading protocol shown in Fig. 4a. For pads M1, M4 and M5, it was found that the damper started sliding for an axial force F_s smaller than the expected one (i.e., $F_s/F_{s,exp} \leqslant 0.88$) because their static friction coefficient was smaller than the nominal value ($0.28 \leqslant \mu_{s1}/\mu_{exp}$[1] $\leqslant 0.61$). This did not hold true for M2 and M3. Indeed, in such a case, $F_s/F_{s,exp} < 1.0$ because the bolt preload sharply decreased during the first loading cycle as depicted in Fig. 5a. This was attributed to a through-thickness deformation of the pads caused by a pore water migration, which occurred in their matrix. Notably, the bolt holes for M2 and M3 were drilled with a water jet cutting machine. Subsequently, the drying phase was performed at a temperature of 40 to 50°C as recommended by the manufacturer. Nevertheless, appreciable water was trapped in the pads' matrix. Part of the initial bolt preload was transferred to the pore water, i.e. the effective stress experienced by the pads' matrix was smaller compared to the applied one. Once the pretension was applied and the pads started sliding, the pore water migrated towards the edges of the pads. This caused a decrease of N_{bolt}. Referring to Fig. 5a, a slight increase of pretension was observed mainly when the applied force F was reversed from tension to compression. Under compression, the sliding outer steel plates moved out-of-plane; this increased the normal stress in the bolts. The preliminary test conducted for $T_{bolt} = 200$ Nm/bolt assisted in adjusting the estimated friction coefficients of the five friction pads in order to conduct the rest of the loading protocols shown in Fig. 4 for $F_{s,exp} = 150$kN and $F_{s,exp} = 300$ kN.

Referring to Table 3, the largest static friction coefficients were obtained for M2 and M3. For $F_{s,exp} = 150$ kN, these were equal to 0.35 and 0.30, respectively. The other materials featured μ_{s1}[2] values between 0.19 and 0.23. A comparison of the μ_{s1} values obtained for $F_{s,exp} = 150$ kN and $F_{s,exp} = 300$ kN reveals that μ_{s1} decreased when the pressure at the sliding interface increased. The effect of the clamping force on μ is further discussed in Section 4.1 of this paper. In accordance with previous findings, a sharp loss of pretension was observed merely for M2 and M3 (i.e., $\Delta N_b > 35\%$ for $F_{s,exp} = 300$ kN). Furthermore, minor variations of F were observed for M4. Indeed, in such a case, N_{bolt} and μ featured a relatively constant value throughout the experiment (i.e., $\Delta N_b = 2\%$ and $\Delta\mu_i \leqslant 9\%$). Conversely, a major variation of F was observed for M1 and M5 during the first loading excursion (i.e., $\Delta F_1 > 20\%$ for $F_{s,exp} = 300$ kN). This was due to the progressive increase of μ as depicted in Table 3 (i.e., $\Delta\mu_i > 20\%$). This relates to the pre-sliding surface conditions of the friction pads. Notably, during the second loading excursion (i.e., once the surface layer of the pads was partially removed), μ slightly varied with the increase of $\sum \delta_i$ (i.e., $\Delta\mu_2 \leqslant 7\%$). Similarly, μ featured relatively constant values for $F_{s,exp} = 150$ kN. This is justified by the fact that the pads utilized for this test were previously tested under two monotonic tests, i.e. at the beginning of the experiment their surface was partially smoothed. Therefore, M1 and M5 provide fairly constant μ values when their surfaces are preliminary scraped.

3.2. Results obtained under Symmetric Cyclic Loading Protocols

This section begins with a qualitative description of the typical friction coefficient evolution and $F-\delta$ response observed under constant/variable pressure and sliding velocity. Pertinent observations regarding temperature are also made. This is followed by a quantitative examination of key experimental data.

3.2.1. Qualitative Performance Evaluation

Figs. 6a and b illustrate the typical friction coefficient evolution under constant displacement amplitude for the two examined pressure levels. For materials whose properties were not particularly affected by the operating temperature (e.g. M4), μ progressively increased with respect to the cumulative displacement due to surface wear [38] (see Fig. 6a). However, under continuous sliding motion, the surface of the pads smoothed; hence, μ stabilized. This process was generally accelerated under high normal pressures, i.e. during most of the tests conducted for $F_{s,exp} = 150$ kN, the stable phase was achieved after a larger number of cycles compared to $F_{s,exp} = 300$ kN.

Referring to Fig. 6b, material M1 exhibited a friction coefficient μ, which increased with respect to the cumulative displacement. Notably,

[1] Ratio between the static friction coefficient obtained at the beginning of the 1st loading excursion and the static or average friction coefficient provided by the manufacturer under a pressure of 1 MPa

[2] Static friction coefficient obtained at the beginning of the 1st loading excursion

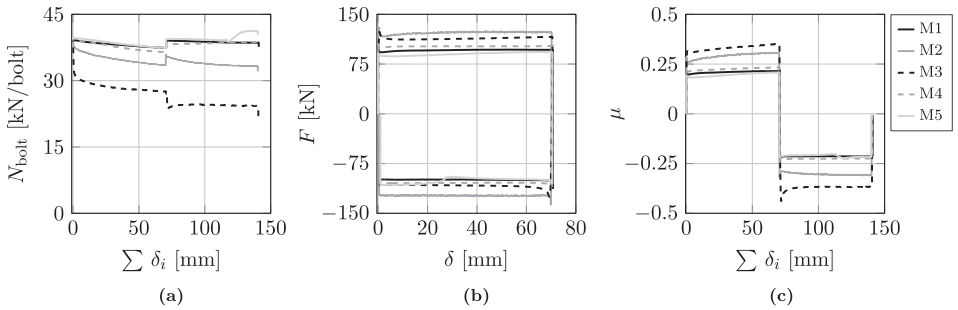

Fig. 5. Results obtained under the linear static loading protocol for T_{bolt} = 200Nm/bolt: (a) bolt preload as a function of the total cumulative displacement, (b) axial force-axial displacement response of the damper, (c) friction coefficient as a function of the total cumulative displacement.

Table 3
Data obtained for $F_{s,exp}$ = 150kN and $F_{s,exp}$ = 300kN under the linear static loading protocol.

	Material ID	Axial force $\frac{F_s^a}{F_{s,exp}^b}$	ΔF_1 [c] [%]	ΔF_2 [%]	Loss of pretension ΔN_b [d] [%]	Friction coefficient μ_{s1} [e]	$\Delta\mu_1$ [f] [%]	$\Delta\mu_2$ [%]
$F_{s,exp}$ = 150kN	M1	0.87	2	13	2	0.19	3	13
	M2	1.16	5	9	22	0.35	10	5
	M3	0.81	7	12	33	0.30	10	9
	M4	0.97	3	6	2	0.23	9	4
	M5	1.12	5	4	2	0.22	7	2
$F_{s,exp}$ = 300kN	M1	0.91	21	6	4	0.17	24	6
	M2	0.64	8	6	36	0.18	33	13
	M3	0.57	4	13	41	0.23	13	5
	M4	0.79	3	4	2	0.18	6	3
	M5	0.86	33	5	1	0.21	38	7

[a]Slip load for $\sum \delta_i$ = 0mm.
[b]Expected slip load estimated with the Coulomb's law of friction and the static friction coefficient provided by the manufacturer (the average friction coefficient is utilized when the static one is not provided)
[c] ΔF_i: maximum axial force variation recorded during the ith loading excursion (estimated compared to the slip load obtained at the beginning of the ith loading excursion)
[d] Total loss of pretension obtained at the end of the test
[e] μ_{si}: static friction coefficient obtained at the beginning of the ith loading excursion
[f] $\Delta\mu_i$: maximum friction coefficient variation obtained during the ith loading excursion (estimated compared to μ_{si})

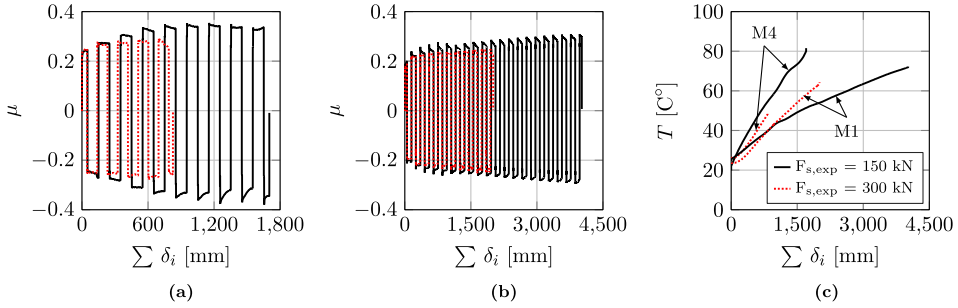

Fig. 6. Cyclic loading protocol with constant amplitude (CA): friction coefficient evolution for (a) M4 and (b) M1, (c) rise in temperature for materials M4 and M1.

the increase observed during the initial loading cycles was attributed to the wearing process. Subsequently, the temperature at the sliding interface progressively increased, thereby causing a steady increase of μ (see Fig. 6b and c). This is discussed in detail in Section 4.2.

Fig. 7 depicts the evolution of the friction coefficient of M4 and M5 under the loading protocols CA and IA. The results suggest that μ is somewhat dependent on the sliding velocity. Notably, during both tests, μ progressively increased during the initial loading cycles and subsequently, stabilized around a relatively constant value (i.e., around 0.28 for M4 and 0.5 for M5 under IA). However, the increased rate was more pronounced for the incremental amplitude protocol. This was in part related to the wearing process, i.e. fragments of the pads piled up at the ends of the grooves and got into the sliding interface once the displacement amplitude was widened. This enhanced the wearing process resulting in an increase of μ at larger displacements [37]. Secondly, the friction coefficient μ may assume larger values at higher loading rates due to visco-plastic phenomena [56]. Referring to Fig. 4c, during the loading protocol with increasing amplitude (f = 0.025 Hz), the sliding velocity v_s is increased by approximately 0.5 mm/s every two loading cycles. Therefore, the observed increase of μ during the first two loading cycles of the experiment was merely due to the wearing process. After the hardening phase, μ became fairly constant regardless of the applied sliding velocity. Therefore, the examined friction pads can provide constant μ values when they operate at v_s values exceeding a

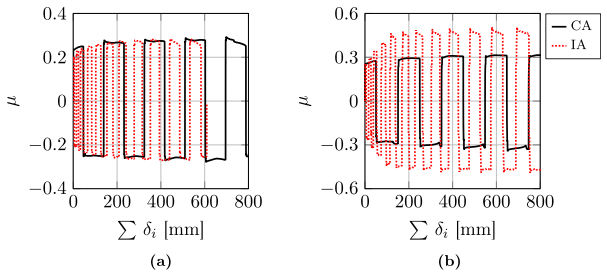

Fig. 7. Friction coefficient evolution under constant (CA) and increasing amplitude at low rate (IA): (a) M4 for $F_{s,exp}$ = 300kN, (b) M5 for $F_{s,exp}$ = 150kN.

given threshold (e.g. around 3 mm/s for M5), i.e. above certain loading rates, the visco-plastic effect becomes negligible.

In cases where the temperature at the sliding interface exceeded 60°C (e.g. see M5), the stable phase was followed by a progressive decrease of μ under consecutive loading cycles (see Fig. 8). Both this and the loading rate effects are further investigated in Section 4.2 of this paper.

Under constant pressure and decreasing sliding velocity (loading protocol DA), the friction coefficient of the materials whose properties were somewhat velocity-dependent evolved as shown in Fig. 9. Notably, for M4, μ progressively increased under decreasing loading velocities for $\sum\delta_i \leqslant 1000$ mm (see Fig. 9a). This suggests that at this stage (i.e., for sliding velocities higher than 4.5 mm/s) the wearing process prevails over the visco-plastic effect leading to an increase of μ. With the progressive decrease of the loading rate, the visco-plastic effect acquires significance, whereas the effects of the wearing process diminish. The combination of these two phenomena leads to a decrease of μ. However, this trend was not observed for M5 in Fig. 9b. Indeed, in this case, μ experienced a sharp increase for $\sum\delta_i > 1500$ mm although decreasing sliding velocities were applied. This was due to the decrease of the bolt preload observed in Fig. 9c up to about 30%, i.e. a pressure decrease occurred at the sliding interface and a consequent increase of μ was observed. Referring to Fig. 10, for friction pads not exhibiting velocity dependency (e.g. M1), μ progressively increased under increasing and decreasing sliding velocities. In such a case, the increase rate, which was comparable to that from constant displacement amplitudes, was attributed to the wearing process and the rise in temperature at the sliding interface. The hardening phase was followed by a stable stage and a softening trend when the heat generated at the sliding interface caused alterations of the pads' surfaces as illustrated in Fig. 11a for M1 and IA-HH. Notably, some coppery areas were clearly visible near the bolt holes. Referring to Fig. 11b, this phenomenon was not observed in other cases due to the gradual increase of T_{surf} (see Fig. 10c).

The data collected for M2 and M3 were obtained under variable pressure. Indeed, consistent with Section 3.1, a sharp loss of pretension was observed during each test performed with M2 and M3 (see Fig. 12a). During the sliding motion, M2 featured a fairly constant μ value because

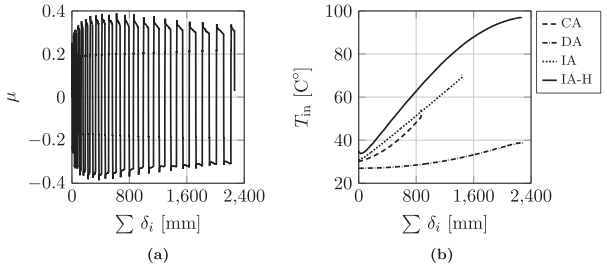

Fig. 8. Results obtained for M5 and $F_{s,exp}$ = 150kN: (a) friction coefficient evolution, (b) rise in temperature tracked with the thermocouples THbolt inside the bolt holes.

(i) the static and dynamic friction coefficient of M2 were relatively similar [13]; and (ii) the contact between the pads' surface and the inner slotted plate slightly varied under consecutive loading cycles. As a result, the pads experienced fairly uniform wear (see Fig. 13a).

Referring to Fig. 13b and d, the pads M3 experienced nonuniform wear and residual bending deformation under the loading protocol CA. This is why the friction coefficient of M3 strongly varied during the sliding motion (see Fig. 13b and d, and F varies once the slip load was exceeded (see Fig. 14a). Conversely, the damper slid under a relatively constant axial force throughout the tests conducted with M4 (see Fig. 14b). Indeed, as illustrated in Fig. 14d, M4 is characterized by similar μ_s and μ_d values. As regards M1 and M5, F mainly varied during the first loading excursion as shown in Fig. 14c. This is consistent with the results obtained under the linear loading protocol (see Fig. 5f) and it corroborates the hypothesis that this relates to the pre-sliding surface conditions of the pads. Indeed, during the second loading excursion (i.e., once the surface layer of the pads was partially removed), μ experienced only slight variations during the sliding motion and the discrepancy between μ_s and μ_d was fairly minor.

Most of the tests carried out with M2, M4 and M5 were terminated due to fracture of at least one friction pad. Fig. 15 shows that fracture extents within the net section normal to the loading direction. During the tests, the thickness of the pads progressively reduced due to the wearing process acting at the sliding interface. Concurrently, the damper axial force remained constant or increased with the number of loading cycles. As a result, the tensile stress demand, which was amplified by stress concentration near the bolt hole, exceeded the tensile stress resistance of the friction pad. Fracture occurred instantaneously in this case.

3.2.2. Quantitative Performance Evaluation

The experimental results obtained under the symmetric cyclic loading protocols for $F_{s,exp}$ = 150 kN and $F_{s,exp}$ = 300 kN are summarized in Tables 4 and 5. Particularly, Table 4 includes (i) the classification of the state of the pads when each test was terminated, (ii) the number of cycles (N_{tot}) and the total cumulative dissipated energy ($\sum E_{tot}$) up to fracture of the friction pad(s), (iii) the maximum measured temperature (T_{max}). On the other hand, Table 5 provides the mean values of F ($\overline{F}$) and μ ($\overline{\mu}$) as well as the total loss of pretension (ΔN_b).

Referring to Table 4, all the tests conducted with M3 were completed. Similarly, for M1, pad's fracture occurred merely during the loading protocol CA for F_s = 300 kN. This represents an isolated case likely caused by the presence of defects arisen during the manufacturing process in the matrix of the composite material M1. The reason why M3 and M1 did not experience fracture under the considered loading protocols is related to the fact that, among all, such pads are characterized by (i) the largest values of tensile/flexural strength and (ii) the smallest values of wear rate.

Conversely, as discussed in Section 3.2.1, most of the tests carried out with M2, M4 and M5 were terminated due to fracture of at least one pad. This phenomenon can be explained by analysing the characteristics of the pads reported in Table 1. Notably, the flexural strength of M5 is approximately 1.3 times lower than the one of M1, whereas its wear rate is 4.5 larger. Similar considerations hold true when the properties of M2 are compared with those of M3. This suggests that M2 and M5 experienced early fracture compared to M3 and M1 due to their high wear rate and low tensile/flexure strength. With regards to M4, its wear rate is approximately half of the one of M5. As a result, M4 fractured after a larger number of cycles compared to M5 although its flexural strength is about 1.8 times smaller.

In most cases, under a constant displacement amplitude (CA), the pads fractured several cycles before those tested under other loading protocols (e.g. IA or DA). This is attributed to the relatively large cumulative energy dissipation demand during CA relative to that of other protocols. For instance, $\sum E_{tot}$ of pad M1 is equal to 680 kJ under CA,

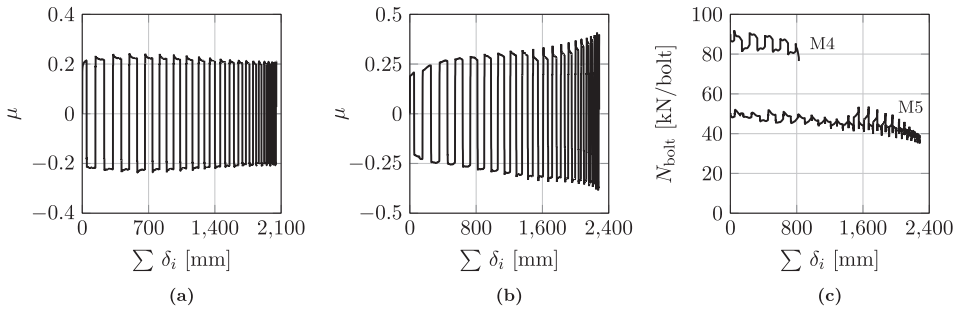

Fig. 9. Results obtained under the cyclic loading protocol with decreasing amplitude (DA): friction coefficient evolution for (a) M4 ($F_{s,exp}$ = 300kN) and (b) M5 ($F_{s,exp}$ = 150kN), (c) bolt preload.

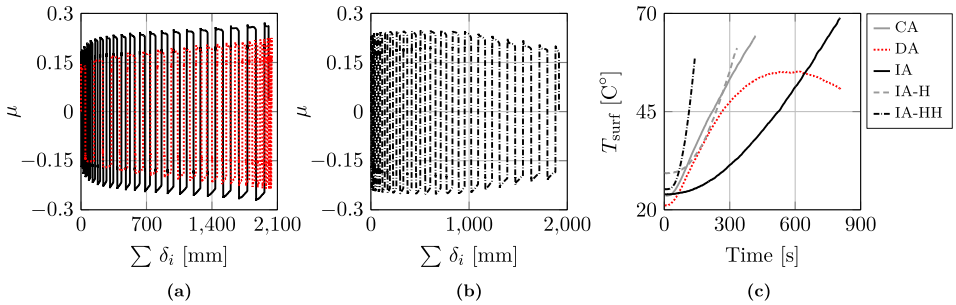

Fig. 10. Results obtained for M1 and $F_{s,exp}$ = 300kN: (a)-(b) friction coefficient evolution, (c) rise in temperature at the surface of the inner slotted plate.

Fig. 11. Surface condition of M1 at the end of the cyclic loading protocol (a) IA-HH and (b) IA for $F_{s,exp}$ = 300kN.

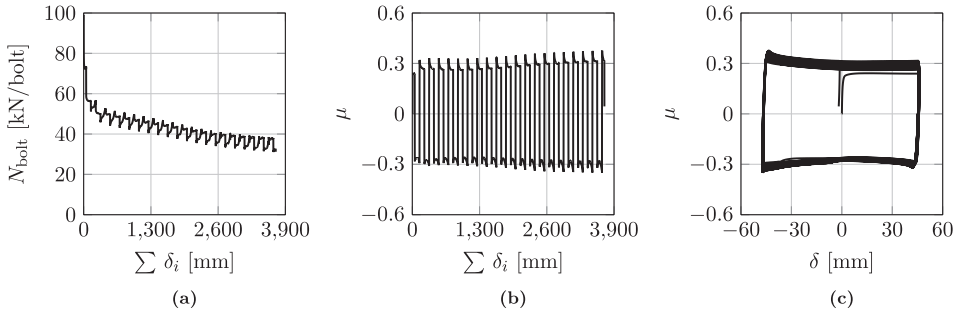

Fig. 12. Results obtained for M3 and $F_{s,exp}$ = 300kN under the cyclic loading protocol with constant amplitude (CA).

whereas it ranges between 310 kJ and 575 kJ for the rest of the loading protocols.

Under continuous sliding, part of the dissipated energy was transformed into heat at the sliding interface [57]. Notably, thermocouples installed close to this zone (see Fig. 3b) recorded T_{max} values above 70°C for M1, M4 and M5, and around 60°C for M2 and M3.

Referring to Table 5, M1 and M4 provide $\overline{\mu}$ values ranging between 0.2 and 0.3, whereas $\overline{\mu} \geqslant 0.30$ is obtained for the rest of the materials. This is explained by the fact that M1 and M4 are characterized by a low wear rate compared to the rest, i.e. the volume of pad's fragments generated at the sliding interfaces is modest. This leads to moderate μ values. However, M1 provides similar $\overline{\mu}$ values under different F_s values and loading rates ($0.19 \leqslant \overline{\mu} \leqslant 0.26$). Moreover, the pretension losses were $\Delta N_b \leqslant 17\%$, thereby yielding to $\overline{F}/F_{s,exp}$ ratios close to 1.0. While pad M4 enjoys comparable $\overline{\mu}$ values with pad M1 ($0.21 \leqslant \overline{\mu} \leqslant 0.32$), several tests were terminated due to early fracture of the pads. As a result, the $\overline{\mu}$ and $\overline{F}$ values of M4 varies within a larger range compared to those of M1. This consideration also applies to M5. However, in such a case, the data set collected for F_s = 300kN is limited compared to the one obtained for F_s = 150 kN due to the early fracture of the pads (see Table 4). Similarly,

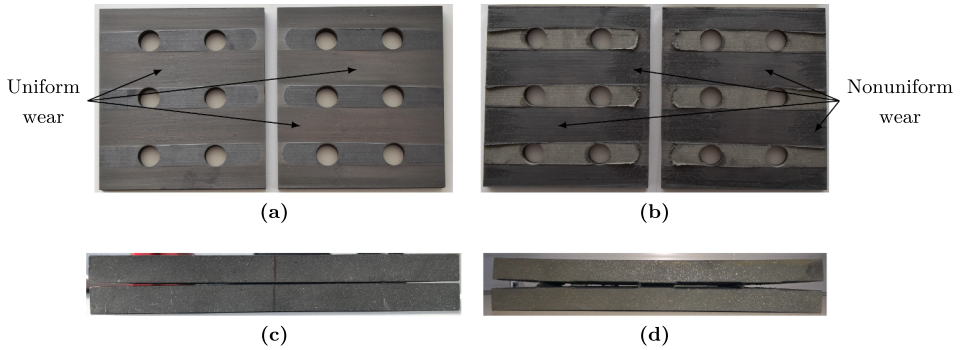

Fig. 13. Condition of (a), (c) M2 and (b), (d) M3 at the end of the cyclic loading protocol (a), (c) IA ($F_{s,exp}$ = 150kN) and (b), (d) CA ($F_{s,exp}$ = 300kN): (a)-(b) surface wearing, (c)-(d) bending deformation.

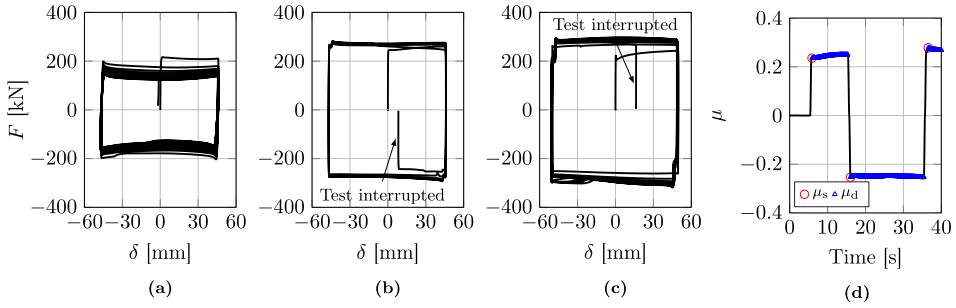

Fig. 14. Results obtained for $F_{s,exp}$ = 300kN under the cyclic loading protocol with constant amplitude (CA): (a) M3, (b) and (d) M4, (c) M1.

Fig. 15. Fracture patterns of the friction pads (a) M2 and (b) M4 at the end of the loading protocol CA for $F_{s,exp}$ = 300kN.

each test performed on M2 for F_s = 300 kN was terminated within the first five loading cycles due to the early fracture of the pads. Conversely, the $\bar{\mu}$ values obtained for M3 suggest that the friction coefficient of M3 is pressure dependent. Indeed, $\bar{\mu}$ shows a reduction of nearly 60% when the clamping force is doubled. Furthermore, most of the $\bar{F}/F_{s,exp}$ ratios obtained for M2 and M3 are well below 1.0. This was attributed to the significant loss of pretension for both M2 ($\Delta N_b > 30\%$) and M3 ($\Delta N_b > 40\%$), which in turn led to major variations of $\bar{\mu}$. As regards M2, noise emissions above 80 dB were recorded throughout the experimental campaign.

Overall, both M1 and M4 demonstrated a satisfactory performance under the employed symmetric cyclic loading protocols. Therefore, further investigations were carried out merely on these two materials with pulse-like and mainshock-aftershock loading protocols. The results are discussed in the following section.

3.3. Performance under Pulse-like and Mainshock-Aftershock Loading Protocols

This section focuses on tests conducted for $F_{s,exp}$ = 300 kN under the pulse-like (PL) and mainshock-aftershock loading protocols (MS-AS) for

Table 4
Number of cycles N_{tot}, total cumulative dissipated energy $\sum E_{tot}$ and maximum temperature T_{max} obtained for $F_{s,exp}$ = 150kN and $F_{s,exp}$ = 300kN.

Protocol ID[a]	Material M1				Material M2				Material M3				Material M4				Material M5			
	St.[b]	N_{tot}	$\sum E_{tot}$ [kJ]	T_{max} [°C]	St.	N_{tot}	$\sum E_{tot}$ [kJ]	T_{max} [°C]	St.	N_{tot}	$\sum E_{tot}$ [kJ]	T_{max} [°C]	St.	N_{tot}	$\sum E_{tot}$ [kJ]	T_{max} [°C]	St.	N_{tot}	$\sum E_{tot}$ [kJ]	T_{max} [°C]
CA	·	20	680	72	x	19	555	58	·	20	475	56	x	9	325	79	x	5	175	50
	x	11	565	64	xx	1	10	32	·	20	465	62	x	5	215	47	xx	3	110	35
IA	·	20	320	50	·	20	305	39	·	20	240	35	xx	15	195	36	x	15	280	63
	·	20	575	68	x	5	30	24	·	20	335	50	x	10	120	40	xx	5	35	25
DA	·	20	310	42	·	20	250	30	·	20	220	34	x	7	180	34	·	20	350	39
	·	20	475	55									·	20	470	62				
IA-H	·	20	340	43	·	20	330	45	·	20	285	58	xx	19	310	79	·	20	450	97
	·	16[c]	270	57	xx	3	15	32	·	20	335	52	·	20	455	68	xx	4	30	31
IA-HH	·	20	560	55									x	8	85	34				

[a] The values reported in the gray rows represent the data obtained for $F_{s,exp}$ = 300kN
[b] State of the pads at the moment of the test termination ([·]: none of the pads fractured, [x]: one pad fractured, [xx]: both pads fractured)
[c] Test terminated due to a oil flow issue with the hydraulic pumps

Table 5
Mean $\overline{F}$, mean $\overline{\mu}$ and total loss of pretension ΔN_b obtained for $F_{s,exp} = 150$kN and $F_{s,exp} = 300$kN under the cyclic loading protocols

Protocol ID[a]	Material M1			Material M2			Material M3			Material M4			Material M5		
	$\frac{\overline{F}}{F_{s,exp}}$	$\overline{\mu}$[b]	ΔN_b [%]	$\frac{\overline{F}}{F_{s,exp}}$	$\overline{\mu}$	ΔN_b [%]	$\frac{\overline{F}}{F_{s,exp}}$	$\overline{\mu}$	ΔN_b [%]	$\frac{\overline{F}}{F_{s,exp}}$	$\overline{\mu}$	ΔN_b [%]	$\frac{\overline{F}}{F_{s,exp}}$	$\overline{\mu}$	ΔN_b [%]
CA	1.15	0.26	4	0.98	0.42	42	0.80			1.28	0.32	18	1.4	0.30	15
	0.95	0.23	11	0.62	0.25	32	0.39	0.26	65	0.90	0.26	9	0.90	0.38	6
IA	0.95	0.19	7	0.94	0.53	53	0.75	0.53	59	1.05	0.25	4	1.54	0.44	17
	0.96	0.23	16	0.71	0.31	48	0.59	0.35	62	0.82	0.25	13	1.00	0.37	2
DA	0.97	0.19	3	0.75	0.35	42	0.64	0.34	38	1.03	0.24	6	1.08	0.30	22
	0.81	0.20	17							0.75	0.21	7			
IA-H	1.01	0.20	0	1.03	0.50	47	0.91	0.44	42	1.12	0.27	9	1.42	0.33	0
	0.91	0.21	7	0.89	0.36	41	0.60	0.30	46	0.77	0.23	16	1.22	0.43	1
IA-HH	1.03	0.23	4							0.94	0.27	7			

[a] The values reported in the gray rows represent the data obtained for $F_{s,exp} = 300$kN
[b] Mean friction coefficient computed by considering both static and dynamic friction coefficients

M1 and M4 pads. Referring to Fig. 16a and d, M1 and M4 provided fairly similar $F-\delta$ responses regardless of the employed loading protocol. Notably, cyclic hardening was observed during the first two loading cycles of PL and MS due to the initial conditions of the friction pad surfaces. Subsequently, F achieved a relatively constant value, which was maintained throughout the loading history. The maximum axial force variation (ΔF_{max}) varied within 15% and 23% for PL and MS and within 6% and 8% for AS1 and AS2. Similar percentages were obtained for $\Delta\mu_{max}$ (i.e., maximum friction coefficient variation). The bolt preload N_{bolt} was fairly constant during each test, thereby indicating no loss of pretension (see Fig. 16b and e). Referring back to Fig. 16c and f, for both M1 and M4, μ progressively increased during the first two loading cycles of PL and MS. This phenomenon was caused by the wearing process on the sliding interfaces. Indeed, it occurred when a relatively constant sliding velocity v_s was applied (i.e., around 10 mm/s) and minor temperature variations were observed. Subsequently, v_s was varied between 27 mm/s and 10 mm/s. Notwithstanding this variation in sliding velocity, μ achieved a constant value for both M1 and M4, which was maintained up to the end of the test; hence, at $v_s > 10$ mm/s the viscoplastic effect became negligible for M4. Similarly, the friction coefficient of M1 did not increase during PL and MS because minor temperature variations occurred during these tests (i.e., less than 1 °C).

Referring to Table 6, the static and dynamic friction coefficients of M1 and M4 were fairly similar ($0.97 \leqslant \overline{\mu}_d/\overline{\mu}_s \leqslant 1.03$). Furthermore, Table 6 reveals that M1 and M4 provide similar $\overline{\mu}$ values during consecutive events. Therefore, under conditions potentially similar to those occurring during a seismic event, the examined friction pads may be suitable for providing supplemental damping in earthquake engineering applications.

4. Discussion

This section provides a discussion on the pressure-dependency of the friction coefficient of M1 and M4. The effect of loading rate, loading history and temperature on μ for M1 and M4 is also debated.

4.1. Pressure Dependency

The mean ($\overline{\mu}$) and standard deviation (σ) of μ are computed for different slip loads and loading protocols as depicted in Fig. 17, where the static and dynamic friction coefficients of the friction pads M1 and M4 are separated. It is apparent that when the clamping force is doubled, $\overline{\mu_s}$ and $\overline{\mu_d}$ experience a maximum variation of approximately 15% for both M1 and M4. Furthermore, the discrepancy between $\overline{\mu_s}$ and $\overline{\mu_d}$ is practically negligible (i.e., $0.95 \leqslant \overline{\mu}_d/\overline{\mu}_s \leqslant 1.00$ for both materials). Therefore, although μ is somewhat pressure dependent, the

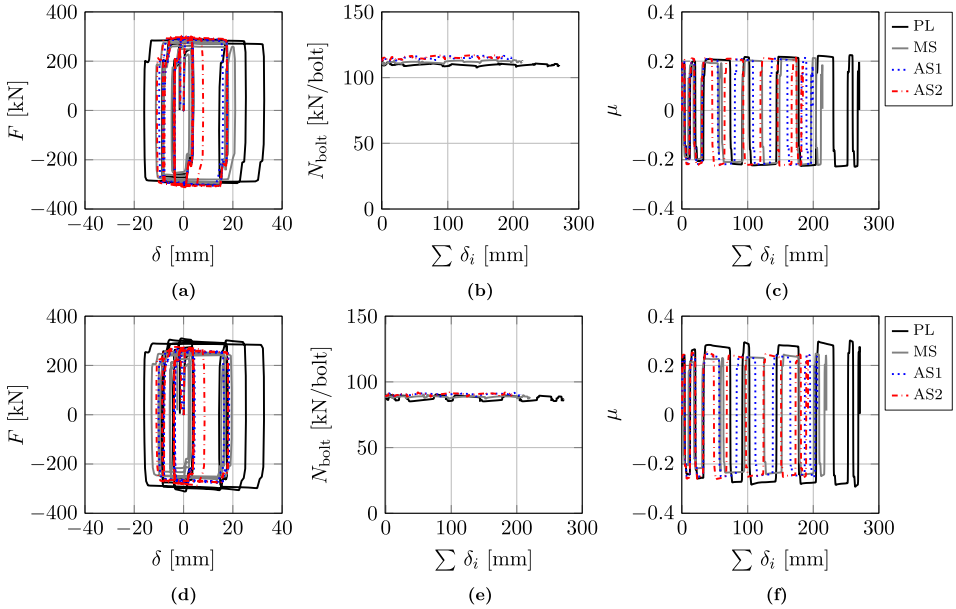

Fig. 16. Results obtained for $F_{exp,s} = 300$kN under the pulse-like (PL) and mainshock-aftershock loading protocol (MS: mainshock, AS1: first aftershock, AS2: second aftershock): (a)-(c) for M1, (d)-(f) for M4.

Table 6
Data obtained for $F_{s,exp} = 300$kN under the pulse-like (PL) and mainshock-aftershock loading protocol (MS: mainshock, AS1: first aftershock, AS2: second aftershock).

Protocol ID	Material M1					Material M4				
	$\frac{\overline{F}^{a}}{F_{s,exp}}$	ΔF_{max} [b] [%]	$\overline{\mu}$ [c]	$\Delta\mu_{max}$ [d] [%]	$\frac{\overline{\mu}_d}{\overline{\mu}_s}$	$\frac{\overline{F}}{F_{s,exp}}$	ΔF_{max} [%]	$\overline{\mu}$	$\Delta\mu_{max}$ [%]	$\frac{\overline{\mu}_d}{\overline{\mu}_s}$
PL	0.95	15	0.22	15	1.01	0.97	20	0.28	19	1.01
MS	0.92	21	0.21	19	1.03	0.82	23	0.23	22	1.02
AS1	0.98	8	0.21	7	0.99	0.87	6	0.24	6	0.97
AS2	0.99	6	0.21	5	0.99	0.89	8	0.24	8	0.97

[a] Mean of the axial force F
[b] Maximum axial force variation recorded during the experiment (estimated compared to $\overline{F}$)
[c] Mean friction coefficient computed by considering both static and dynamic friction coefficients
[d] Maximum friction coefficient variation recorded during the experiment (estimated compared to $\overline{\mu}$)

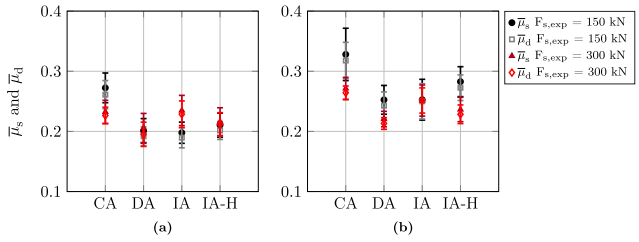

Fig. 17. Mean of μ_s and μ_d obtained for different expected slip loads and loading protocols (CA: constant amplitude; DA: decreasing amplitude; IA, IA-H, IA-HH: increasing amplitude at low, moderate and high rate; PL: pulse-like, MS: mainshock; AS1: first aftershock; AS2: second aftershock): (a) for M1, (b) for M4.

corresponding percentage reductions of $\overline{\mu}$ are fairly modest at pressures higher than 7 MPa - 8 MPa. Referring to Fig. 17, σ assumes values smaller than 0.05 regardless of the employed loading protocol and pressure level. Noteworthy stating that part of this variability is due to the surface damage of the inner steel plate. Indeed, while it was designed with a higher hardness than that of the friction pads, the surface of the steel plate exhibited some damage due to wear after numerous cyclic loading tests. However, this source of variability is deemed negligible.

4.2. Effect of Loading Rate, Loading History and Temperature

Figs. 18a and d illustrate the friction coefficients obtained under different loading protocols and sliding velocities v_s for $F_{s,exp} = 300$kN. For M1, it is apparent that μ is not particularly affected by the imposed sliding velocity. For M4, while μ attains a small increase up to $v_s < 10$mm/s, this is not statistically significant. According to [58], it is reasonable to assume that M4 is characterized by a visco-plastic shear strength; hence its stress–strain response varies according to the imposed deformation rate [59]. While the friction coefficient of M4 turns out to be somewhat loading-rate dependent [56], this dependency vanishes at sliding velocities $v_s > 10$mm/s. Therefore, under conditions potentially similar to those occurring during a seismic event, M4 can provide relatively stable μ values.

With regard to the temperature effect, Fig. 18c and f illustrate the friction coefficients of M1 and M4 as a function of the temperature tracked at the surface of the inner slotted plate (T_{surf}) for $F_s = 300$kN and the examined loading protocols. It is likely that the T_{surf} values associated to μ in Fig. 18c and f are somewhat lower compared to the effective temperature experienced by the pads at the sliding interface. Referring to Fig. 18c, the rise from room temperature to 40°C causes a modest increase of μ. However, under IA-HH, μ progressively decreases for $T_{surf} > 40$°C. As discussed in Section 3.2.1, this phenomenon is attributable to the surface alteration of the pads caused by the heat generated at the sliding interface (see Fig. 11). Conversely, the experimental results obtained for M4 suggest that its friction coefficient is practically

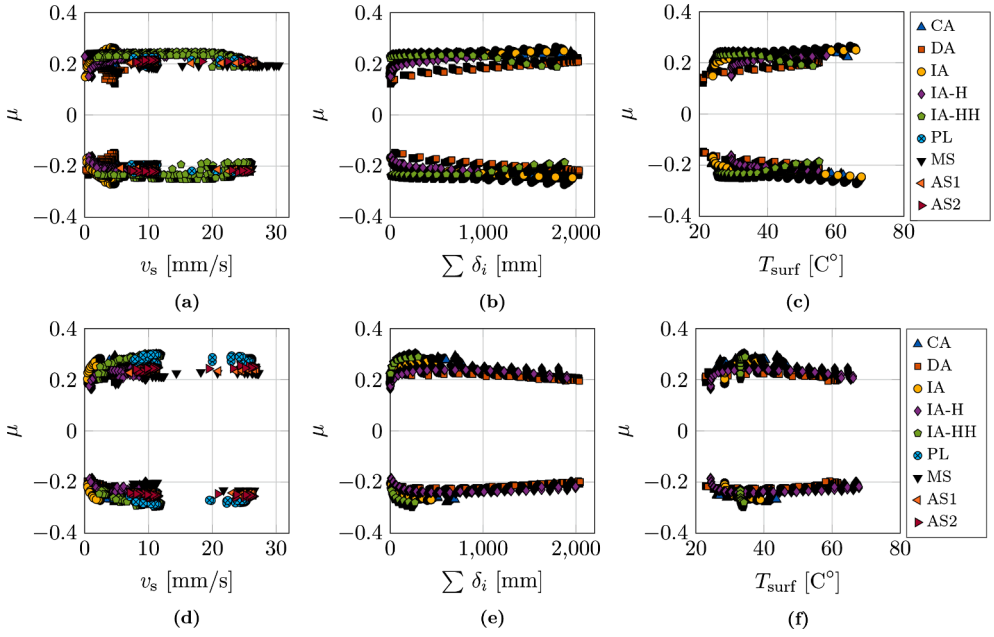

Fig. 18. Friction coefficient obtained for (a)-(c) M1 and (d)-(f) M4 under different loading protocols and $F_{s,exp} = 300$kN.

insensitive to the increase of T_{surf}.

5. Conclusions

This paper presents findings from a comprehensive experimental program conducted on a prototype sliding friction damper that was developed within the Resilient Steel Structures Laboratory at EPFL. The tests featured five non-metallic composite friction pads (termed M1 to M5 herein) at two different pressure levels through bolt pretension and under monotonic and cyclic loading protocols. Their static and dynamic friction coefficients were properly quantified in order to evaluate the applicability of the examined friction pads in providing supplemental damping in frame structures during earthquake shaking.

A number of shortcomings have been encountered with materials M2, M3 and M5. Particularly, pads made of M2 exhibited noise emissions above 80 dB. Moreover, at a sliding force of $F_{s,exp} = 300$kN most of the tests were terminated after a few cycles due to net section fracture of the pads near their bolt holes. Same limitations hold true for M5. Conversely, the friction coefficient of M3 proved to be pressure dependent.

Cyclic tests with pads made of materials M2 and M3 demonstrated a significant loss of bolt pretension. This caused variation in contact between the pads and the inner slotted plate. As a result, pads M3 usually experienced nonuniform wear and an irreversible bending deformation. The observed loss of pretension was mainly attributable to the inadequate dry treatment carried out on pads made of M2 and M3 after drilling the bolt holes with a water jet machine. Therefore, the performance of these two materials may be re-evaluated provided that a different manufacturing technique is employed.

In contrast, the prototype friction damper performed satisfactory when the friction pads featured materials M1 and M4. Particularly, both materials were characterized by similar static and dynamic friction coefficients (i.e., $0.95 \leqslant \overline{\mu}_d/\overline{\mu}_s \leqslant 1.00$). Consequently, the friction damper exhibited a fairly stable axial force - axial displacement hysteretic response without variations in axial force demands.

The experimental results suggest that the friction coefficient of pads M1 and M4 was fairly invariant at pressures higher than 7 to 8MPa. These are typical for the range of slip loads to be achieved with friction dampers in seismic applications.

A comprehensive assessment of the μ values obtained for pads M1 and M4 under various loading histories reveals that both materials provide fairly consistent μ values when they operate at sliding velocities larger than 10 mm/s. Furthermore, the friction coefficient of pads M4 is practically insensitive to temperature variations measured during tests (i.e., roughly between 20 °C and 70 °C). On the contrary, the friction coefficient of M1 tends to slightly increase with the rise in temperature at the sliding interface. However, the experimental results obtained under the pulse-like and mainshock-aftershock loading protocols suggest that under conditions somewhat similar to those occurring during a seismic event, the temperature at the sliding interface does not increase sufficiently to cause major variations of μ. Furthermore, μ assumes similar values under consecutive events for both materials.

The pad surfaces were fairly damaged due to surface wear regardless of the imposed loading history. While surface wear often caused net section fracture to the pads during loading histories imposing cumulative energies of more than 85kJ, this issue can be easily addressed by simply using thicker friction pads.

In conclusion, the results suggest that friction pads M1 and M4 are promising for further exploitation in sliding friction dampers for earthquake-induced vibration control of structures.

Finally, the experimental program summarized in this paper features a number of limitations. First, the pressure- and velocity-dependency of the pads' friction coefficient was investigated for a maximum pressure level of approximately 20 MPa and a maximum sliding velocity of 30 mm/s. These limits were imposed by the capacity of the existing laboratory equipment. Future experiments should be conducted with emphasis at larger input velocities characteristic of near-fault earthquake sequences. Moreover, time-dependent phenomena associated with force relaxations should also be carefully evaluated with the examined materials.

Data availability statement

Some or all data generated or used during the study are available in a repository or online in accordance with funder data retention policies. Some or all data that support the findings of this study can be publicly accessed from Zenodo data repository 10.5281/zenodo.4544314 or can be made available from the corresponding author upon reasonable request.

Declaration of Competing Interest

The authors declare that they have no known competing financial interests or personal relationships that could have appeared to influence the work reported in this paper.

Acknowledgements

This study is based on work supported by the Swiss National Science Foundation (Project No. 200021_188476). The financial support is gratefully acknowledged. Any opinions, findings and conclusions expressed in the paper are those of the authors and do not necessarily reflect the views of sponsors. The authors would like to sincerely thank the technical staff at the EPFL Structures Laboratory: Lea Frederique Dubugnon, Gilles Guignet and Serge Despont, as well as the undergraduate students: Cesar Daniel Ramirez Mendoza (summer intern from University of Texas at El Paso, USA), Nitesh Karmacharya (intern from University of Katmandu, Nepal) and graduate student Elias Merhi (EPFL, Switzerland) for their invaluable assistance during the testing program.

References

[1] Soong T, Spencer B. Supplemental energy dissipation: State-of-the-art and state-of-the-practice. Engineering Structures - ENG STRUCT 2002;24:243–59. https://doi.org/10.1016/S0141-0296(01)00092-X.
[2] Symans M, Charney F, Whittaker A, Constantinou M, Kircher C, Johnson M, et al. Energy dissipation systems for seismic applications: current practice and recent developments. Journal of structural engineering 2008;134(1):3–21.
[3] Merritt S, Uang C.M., Benzoni G. Subassemblage testing of star seismic buckling-restrained braces. Rep No TR-2003 2003;4.
[4] Black CJ, Makris N, Aiken ID. Component testing, seismic evaluation and characterization of buckling-restrained braces. ASCE Journal of Structural Engineering 2004;130(6):880–94.
[5] Fahnestock LA, Ricles JM, Sause R. Experimental evaluation of a large-scale buckling-restrained braced frame. ASCE Journal of Structural Engineering 2007; 133(9):1205–14.
[6] Kiggins S, Uang CM. Reducing residual drift of buckling-restrained braced frames as a dual system. Eng. Struct. 2006;28(11):1525–32.
[7] Erochko J, Christopoulos C, Tremblay R, Choi H. Residual drift response of smrfs and brb frames in steel buildings designed according to asce 7–05. ASCE Journal of Structural Engineering 2010;137(5):589–99.
[8] Constantinou M.C, Symans M. Experimental and analytical investigation of seismic response of structures with supplemental fluid viscous dampers. Ph.D. thesis; State University of New York at Buffalo; 1992.
[9] Makris N, Roussos Y, Whittaker A, Kelly J. Viscous heating of fluid dampers during seismic and wind excitations: analytical solutions and design formulae. Earthquake Engineering Research Center, University of California at Berkeley, Berkeley, CA Report No UCB/EERC 1997;:97–11.
[10] Black C.J, Makris N. Viscous heating of fluid dampers under wind and seismic loading: experimental studies, mathematical modeling and design formulae. Earthquake Engineering Resource Center, College of Engineering, the University of California, Berkeley; 2005.
[11] Ferri A. Friction damping and isolation systems. Journal of Vibration and Acoustics 1995;117(B):196–206.
[12] Christopoulos C, Filiatrault A. Principles of passive supplemental damping and seismic isolation. IUSS Press; 2005.
[13] Pall A.S. Limited slip bolted joints: a device to control the seismic response of large panel structures. Ph.D. thesis; Concordia University; 1979.
[14] Filiatrault A, Tremblay R, Kar R. Performance evaluation of friction spring seismic damper. Journal of Structural Engineering 2000;126(4):491–9.

[15] Pall AS, Marsh C. Response of friction damped braced frames. ASCE Journal of Structural Engineering 1982;108(9):1313–23.
[16] Filiatrault A, Cherry S. Performance evaluation of friction damped braced steel frames under simulated earthquake loads. Earthquake Spectra 1987;3(1):57–78.
[17] Aiken I.D, Kelly J, Pall A. Seismic response of a nine-story steel frame with friction damped cross-bracing. In: Proceedings, 9th world conference on earthquake engineering, Tokyo and Kyoto, Japan. 1988,.
[18] Aiken I, Kelly J. Earthquake simulator testing and analytical studies of two energy-absorbing systems for multistory structures. Ph.D. thesis; Berkeley University of California; 1990.
[19] Aiken ID, Nims DK, Whittaker AS, Kelly JM. Testing of passive energy dissipation systems. Earthquake spectra 1993;9(3):335–70.
[20] Fitzgerald T, Anagnos T, Goodson M, Zsutty T. Slotted bolted connections in aseismic design for concentrically braced connections. Earthquake Spectra 1989;5 (2):383–91.
[21] Grigorian CE, Yang TS, Popov EP. Slotted bolted connection energy dissipators. Earthquake Spectra 1993;9(3):491–504.
[22] Tremblay R. Seismic behavior and design of friction concentrically braced frames for steel buildings. Ph.D. thesis; University of British Columbia; 1993.
[23] Yang T.S, Popov E.P. Experimental and analytical studies of steel connections and energy dissipators. Earthquake Engineering Research Center, University of California; 1995.
[24] Tirca L, Serban O, Tremblay R, Jiang Y, Chen L. Seismic design, analysis and testing of a friction steel braced frame system for multi-storey buildings in vancouver. In: Key Engineering Materials; vol. 763. Trans Tech Publications Ltd; 2018, p. 1077–1086.
[25] Mualla IH, Belev B. Performance of steel frames with a new friction damper device under earthquake excitation. Eng. Struct. 2002;24(3):365–71.
[26] LIAO W.I, MUALLA I, LOH C.H. Shaking-table test of a friction-damped frame structure. The Structural Design of Tall and Special Buildings 2004;13(1):45–54.
[27] Leung H, Clifton G, Khoo H.H, Macrae G. Experimental studies of eccentrically braced frame with rotational active links. In: 8th international conference on behavior of steel structures in seismic areas, Shanghai, China. 2015,.
[28] Clifton G.C. Semi-rigid joints for moment-resisting steel framed seismic-resisting systems. Ph.D. thesis; ResearchSpace@ Auckland; 2005.
[29] MacRae GA, Clifton GC, Mackinven H, Mago N, Butterworth J, Pampanin S. The sliding hinge joint moment connection. Bulletin of the New Zealand Society for Earthquake Engineering 2010;43(3):202–12.
[30] Latour M, Piluso V, Rizzano G. Free from damage beam-to-column joints: Testing and design of dst connections with friction pads. Eng. Struct. 2015;85:219–33.
[31] Morgen B. A friction damper for post-tensioned precast concrete moment frames. PCI Journal 2004;49. doi: 10.15554/pcij.07012004.112.133.
[32] Kim HJ, Christopoulos C. Friction damped posttensioned self-centering steel moment-resisting frames. Journal of Structural Engineering 2008;134(11): 1768–79.
[33] Iyama J, Seo C, Ricles J, Sause R. Self-centering mrfs with bottom flange friction devices under earthquake loading. J. Constr. Steel Res. 2009;65(2):314–25.
[34] Borzouie J, MacRae G, Chase J, Rodgers G, Clifton G. Experimental studies on cyclic performance of column base strong axis–aligned asymmetric friction connections. Journal of Structural Engineering 2016;142(1):04015078.
[35] Freddi F, Dimopoulos CA, Karavasilis TL. Rocking damage-free steel column base with friction devices: design procedure and numerical evaluation. Earthquake Engineering & Structural Dynamics 2017;46(14):2281–300.
[36] Golondrino J.C, MacRae G, Clifton C. Behaviour of asymmetrical friction connections using different shim materials. In: Proceedings of the New Zealand Society for Earthquake Engineering Conference. 2012a,.
[37] Khoo HH, Clifton C, Butterworth J, MacRae G, Ferguson G. Influence of steel shim hardness on the sliding hinge joint performance. J. Constr. Steel Res. 2012;72: 119–29.
[38] Latour M, Piluso V, Rizzano G. Experimental analysis on friction materials for supplemental damping devices. Constr. Build. Mater. 2014;65:159–76.
[39] Rojas P, Ricles J, Sause R. Seismic performance of post-tensioned steel moment resisting frames with friction devices. Journal of Structural Engineering 2005;131 (4):529–40.
[40] Wolski M, Ricles JM, Sause R. Experimental study of a self-centering beam–column connection with bottom flange friction device. Journal of Structural Engineering 2009;135(5):479–88.
[41] Ono S, Nakahira K, Tsujioka S, Uno N. Energy absorption capacity of thermally sprayed aluminum friction dampers. J. Therm. Spray Technol. 1996;5(3):303–9.
[42] Latour M, Piluso V, Rizzano G. Experimental analysis and design of friction joints equipped with sprayed aluminum dampers. In: Proceedings of the 8th International Workshop on Connections in Steel Structures, Boston, USA, May. 2016, p. 619–630.
[43] Wolff E.D. Frictional heating in sliding bearings and an experimental study of high friction materials. Ph.D. thesis; State University of New York at Buffalo; 1999.
[44] Kim H, Christopoulos C, Tremblay R. Experimental characterization of boltstressed non asbestos organic (nao) material-to-steel interfaces. Report, Dept of Civil Engineering, University of Toronto, Canada 2004;:6–30.
[45] Golondrino J.C., MacRae G, Chase J, Rodgers G, Clifton C. Clamping force effects on the behaviour of asymmetrical friction connections (afc). In: Proceedings of the 15th World Conference on Earthquake Engineering (15WCEE), Lisbon, Portugal, September. 2012b, p. 24–28.
[46] Tsampras G, Sause R. Development and experimental validation of deformable connection for earthquake-resistant building systems with reduced floor accelerations. Network of Earthquake Engineering Simulation (NEES) Technical Report, https://nees org/resources/13612 2015;.
[47] SIA 263. Steel structures. Swiss Society of Engineers and Architects (SIA), Zurich; 2013.
[48] Eurocode 3. Design of steel structures. British Standards Institution (BSI), London; 2005.
[49] Persson B.N. Sliding friction: physical principles and applications. Springer Science & Business Media; 2013.
[50] Rabinowicz E. Friction and wear of materials. 2 ed. New York: Wiley & Sons; 1995.
[51] Standard D639-14. Standard Test Method for Tensile Properties of Plastics. West Conshohocken, PA, USA: American Society for Testing and Materials (ASTM); 2014.
[52] Standard D695-15. Standard Test Method for Compressive Properties of Rigid Plastics. West Conshohocken, PA, USA: American Society for Testing and Materials (ASTM); 2015.
[53] Standard D790-03. Standard Test Method for Flexural Properties of Unreinforced and Reinforced Plastics and Electrical Insulating Materials. West Conshohocken, PA, USA: American Society for Testing and Materials (ASTM); 2003.
[54] Alavi B, Krawinkler H. Behavior of moment-resisting frame structures subjected to near-fault ground motions. Earthquake Engineering & Structural Dynamics 2004; 33(6):687–706.
[55] Gordo-Monsó C, Miranda E. Significance of directivity effects during the 2011 lorca earthquake in spain. Bull. Earthq. Eng. 2018;16(7):2711–28.
[56] Lemaitre J. Handbook of Materials Behavior Models, Three-Volume Set: Nonlinear Models and Properties. Elsevier; 2001.
[57] Bhushan B. Modern tribology handbook, Two volume set. CRC Press 2000.
[58] Bowden F.P, Tabor D. Friction: an introduction to tribology. RE Krieger Publishing Company; 1973.
[59] François D, Pineau A, Zaoui A. Mechanical behaviour of materials: Volume II: Viscoplasticity, Damage, Fracture and Contact Mechanics. Springer Science & Business Media; 1998.